

See discussions, stats, and author profiles for this publication at: <https://www.researchgate.net/publication/344526305>

Guidelines for System Identification of Multirotor Vehicles with Highly Correlated Inputs

Conference Paper · October 2020

DOI: 10.4050/F-0076-2020-16294

CITATIONS

4

READS

746

4 authors, including:



[Tom Berger](#)
U.S. Army Combat Capabilities Development Command Aviation & Missile Center
91 PUBLICATIONS 929 CITATIONS

[SEE PROFILE](#)



[Mark Joseph Santos Lopez](#)
San Jose State University Research Foundation
20 PUBLICATIONS 172 CITATIONS

[SEE PROFILE](#)



[Mark B. Tischler](#)
US Army Aviation Development Directorate - AFDD
191 PUBLICATIONS 3,882 CITATIONS

[SEE PROFILE](#)

Guidelines for System Identification of Multirotor Vehicles with Highly Correlated Inputs

Tom Berger

Aerospace Engineer

U.S. Army Combat Capabilities Development
Command Aviation & Missile Center
Moffett Field, CA, USA

Aaron M. Wagner

Research Intern

San Jose State University
Santa Clara University
Moffett Field, CA, USA

Mark J. S. Lopez

Aerospace Engineer

U.S. Army Combat Capabilities Development
Command Aviation & Missile Center
Moffett Field, CA, USA

Mark B. Tischler

Senior Technologist

U.S. Army Combat Capabilities Development
Command Aviation & Missile Center
Moffett Field, CA, USA

ABSTRACT

With the development of new over-actuated multirotor vertical lift aircraft, there is a need to identify accurate vehicle models from flight data at the individual effector level to validate physics based models or skip physics based models altogether and develop simulation models direction from the identification results. Typical frequency-domain system identification methods break down when the bare-airframe inputs are highly correlated, which is often the case when collecting system identification data for over-actuated vehicles. The Joint Input-Output Method has been previously used to mitigate the issue of input correlation, and is applied in this paper to a simulation example based on an octocopter UAS in hover. Several excitation methods are investigated to determine which are best suited for use with the Joint Input-Output Method. The identification results of the different methods with varying levels of measurement noise are presented, as are the main advantage and disadvantages of each method. Based on these results, guidelines are provided for multirotor system identification using the Joint Input-Output Method.

NOTATION

Symbols

C	Control allocation matrix
F	Feed-forward controller
G_{xx}	Power spectral density matrix
G_{xy}	Cross spectral density matrix
H_{xy}	Frequency response (matrix) from inputs in vector x to outputs in vector y
K	Feedback controller
M	Virtual effector to individual actuator mixing matrix
N	Individual actuator to virtual effector mixing matrix
n	Vector of measurement noise
P	Bare-airframe
r	Vector of reference inputs

u	Vector of tracking signal commands
v	Vector of commands summed into bare-airframe inputs
x	Vector of bare-airframe inputs
y	Vector of bare-airframe outputs
γ_{xy}^2	Coherence between x and y
ω	Frequency [rad/sec]
σ_n	Noise RMS value
\tilde{v}	Vector of commands summed into virtual effectors inputs
\tilde{x}	Vector of virtual effector inputs

Acronyms

NSR	Noise-to-Signal Ratio
PSD	Power Spectral Density
SNR	Signal-to-Noise Ratio

Presented at the VFS 76th Annual Forum & Technology Display, October 6–8, 2020, Virtual. This is work of the U.S. Government and is not subject to copyright protection in the U.S. Distribution Statement A. Approved for public release; distribution is unlimited.

INTRODUCTION

The new generation of vertical lift aircraft, including the U.S. Army's Future Attack Reconnaissance Aircraft (FARA) and Future Long Range Assault Aircraft

(FLRAA) as well as manned urban air mobility (UAM) and unmanned multirotor electric vertical take-off and landing (eVTOL) configurations, are generally over-actuated with more controls (e.g., swashplate actuators, aerosurface actuators, motor RPM commands, etc.) than command variables (e.g., roll rate, pitch rate, yaw rate, and thrust). System identification models for such aircraft need to accurately represent the bare-airframe with explicit control derivatives determined for each individual control effector or actuator. Such models are needed for physics-based simulation model validation and control system design including control allocation design for nominal operation and control reconfiguration algorithms in the case of failed control actuators (e.g., Ref. 1).

Frequency-domain system identification methods used to characterize the bare-airframe require that the bare-airframe inputs be at most partially correlated (with cross-control coherence of $\gamma^2 < 0.5$) (Ref. 2). In the case of over-actuated vertical lift aircraft, system identification data are typically collected with a control system engaged and with a fixed control allocation scheme, which can lead to fully correlated bare-airframe inputs even when the bare-airframe dynamics are decoupled. Tischler (Ref. 2) provides a Multi-Input/Single-Output (MISO) Direct Method to condition the data and remove the effects of partially-correlated secondary inputs, however, the method breaks down for highly- or fully-correlated inputs (cross-control coherence of $\gamma^2 > 0.5$).

Berger, et al. (Ref. 3) addressed the issue of fully correlated inputs in flight dynamics system identification by employing the Joint Input-Output (JIO) Method as a post-processing step to the MISO Direct Method, and showed that accurate identification results of a Multi-Input/Multi-Output (MIMO) bare-airframe can be obtained in the presence of fully-correlated inputs.

In the JIO Method, both the inputs and outputs of the bare-airframe are considered jointly as outputs to a set of uncorrelated (or at most partially-correlated) reference inputs. The identification is still done using the standard MISO Direct Method, and results in two sets of identified frequency responses: 1) from reference inputs to bare-airframe inputs, and 2) from reference inputs to bare-airframe outputs. The bare-airframe frequency responses are then calculated from the ratio of the frequency responses identified using the MISO Direct Method.

The JIO Method was first proposed by Akaike in 1967 (Ref. 4) as a way to mitigate measurement noise correlation when analyzing single-input/single-output (SISO) systems with feedback, and is based on the time-domain Instrumental Variables Method introduced by Geary (Ref. 5) and Reiersøl (Ref. 6) in the 1940s in the field of econometrics. In the 1970s, work was done on assessing the accuracy of results obtained using the JIO

Method (e.g., Ref. 7,8) and on extending its use to parametric MIMO system identification (e.g., Refs. 9–11). In the 1980s, work continued on extending the JIO Method to non-parametric (frequency response) MIMO system identification (e.g., Refs. 12,13). At the same time, the JIO Method also began being used in the field of modal analysis and referred to as the Three-Channel Frequency Response Function (FRF) Method (e.g., Refs. 14–16).

More recently, the JIO Method was utilized by Gennaretti (Ref. 17) and Hersey (Ref. 18) for identification of rotorcraft inflow models with highly-correlated inputs. Hersey also introduced a method to estimate the coherence for frequency responses identified using the JIO Method. The JIO Method has also recently been applied to identify flight-dynamics models of several aircraft from flight data, including an F-16 (Ref. 19), a business jet (Refs. 3,20), an octocopter unmanned aerial system (UAS) (Refs. 20,21), and the Bell V-280 tiltrotor aircraft (Ref. 22). In all four cases, the flight data were collected closed-loop, which resulted in the bare-airframe inputs being highly correlated. In the case of the F-16 (Ref. 19), the octocopter (Refs. 20,21), and the V-280 (Ref. 22), the aircraft had redundant controls which further led to high correlation between redundant inputs in each axis. In all cases, the JIO Method was successfully applied to identify accurate bare-airframe models from flight data with correlated inputs.

In this paper, a closed-loop simulation example of an octocopter UAS is used to investigate the effects of different JIO strategies on the identification results. Specifically, the choices of vehicle excitation input location, bare-airframe input selection, and reference signal selection, are investigated. For example, for vehicles operating in closed-loop, excitation signals may be summed into the closed-loop tracking command or directly into the bare-airframe inputs. In the first case, the control system attempts to track the excitation signal, while in the latter the control system sees the excitation signal as a disturbance and attempts to reject it. In the case of bare-airframe input selection, the choice is between individual actuators or virtual effectors, which can be formed from symmetric and differential groups of actuators to concentrate the vehicle excitation to a particular axis. For example, for a winged aircraft with individual actuators consisting of left and right flaperons, virtual effectors consisting of symmetric and differential flaperons can be excited to produce primarily pitch and roll motion. Finally, the reference signal used in the analysis can be any signal measured that has high coherence with both the bare-airframe inputs and the bare-airframe outputs. However, external signals that are not correlated with the noise in the system are often the best choice for reference signals, since they produce unbiased estimates (Ref. 4).

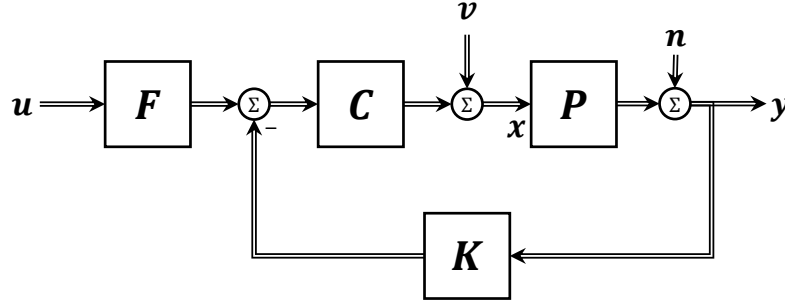


Fig. 1. Generic closed-loop block diagram representative of a multirotor vehicle.

The remainder of the paper is organized as follows. First, a brief overview of multi-input system identification is given, with descriptions of the MISO Direct and JIO Methods. Next, the test case used in this paper is described, including the bare-airframe and control system. The different JIO strategies investigated in the paper are then introduced, and predicted analytical results are given for each method to demonstrate the difference between them. This is followed by the simulation identification results for the different JIO strategies, which are correlated with the analytical results. Finally, a discussion of the results, including guidelines for system identification of multirotor UAS, and conclusions are presented.

MULTI-INPUT SYSTEM IDENTIFICATION USING THE JOINT INPUT-OUTPUT METHOD

Multi-Input System Identification Overview

Figure 1 shows a generic block diagram that is representative of a multirotor vehicle and consists of a MIMO bare-airframe \mathbf{P} , control allocation \mathbf{C} (sometimes referred to as mixer or effector blender), feedback controller \mathbf{K} , and feed-forward controller \mathbf{F} . The tracking command inputs (generated by the pilot stick or ground station) are denoted by vector $\mathbf{u} \in \mathbb{R}^{n_u}$, bare-airframe inputs by vector $\mathbf{x} \in \mathbb{R}^{n_x}$, bare-airframe outputs by vector $\mathbf{y} \in \mathbb{R}^{n_y}$, and measurement noise by vector $\mathbf{n} \in \mathbb{R}^{n_y}$. Inputs $\mathbf{v} \in \mathbb{R}^{n_x}$ may also be summed directly into the bare-airframe inputs to excite the vehicle.

A non-parametric frequency-response matrix representation of the MIMO bare-airframe \mathbf{P} is necessary for parametric model structure determination and for transfer-function and state-space model identification. The MIMO bare-airframe \mathbf{P} can be expressed as a matrix of frequency responses:

$$\mathbf{P} = \begin{bmatrix} H_{x_1 y_1}(\omega) & \dots & H_{x_n y_1}(\omega) \\ \vdots & \ddots & \vdots \\ H_{x_1 y_n}(\omega) & \dots & H_{x_n y_n}(\omega) \end{bmatrix} \quad \mathbf{H}_{xy}(\omega) \quad (1)$$

which can be identified from flight data by exciting the bare-airframe through some external excitation (e.g., \mathbf{u} or \mathbf{v} in Fig. 1), and measuring \mathbf{x} and \mathbf{y} . The responses of \mathbf{x} and \mathbf{y} to the external signals in Fig. 1 are given by:

$$\begin{aligned} \mathbf{y} &= (\mathbf{I} + \mathbf{PCK})^{-1} \mathbf{PCFu} + (\mathbf{I} + \mathbf{PCK})^{-1} \mathbf{Pv} \\ &\quad + (\mathbf{I} + \mathbf{PCK})^{-1} \mathbf{n} \\ \mathbf{x} &= (\mathbf{I} + \mathbf{CKP})^{-1} \mathbf{CFu} + (\mathbf{I} + \mathbf{CKP})^{-1} \mathbf{v} \\ &\quad + (\mathbf{I} + \mathbf{CKP})^{-1} \mathbf{CKn} \end{aligned} \quad (2)$$

Using the frequency-domain Multi-Input/Single-Output (MISO) Direct Method (Ref. 2), the bare-airframe frequency-response matrix \mathbf{H}_{xy} can be identified from the input \mathbf{x} and output \mathbf{y} auto- and cross-spectral density matrices as:

$$\mathbf{H}_{xy}(\omega) = \mathbf{G}_{xy}(\omega) \mathbf{G}_{xx}^{-1}(\omega) \quad (3)$$

Equation 3 represents $n_y \times n_x$ matrix at each of the n_ω frequency points used in the analysis. In CIFER® (Ref. 2) for example, the spectral density functions ($G_{x_i y_j}$ and $G_{x_i x_j}$) that make up the spectral density matrices in the right-hand side of Eq. 3 are first extracted from overlapped windowed time history data, using several different window lengths. Then, the calculation in Eq. 3 is applied one output at a time to produce conditioned frequency responses. Finally, the conditioned frequency responses from the different window lengths are combined into composite frequency responses.

When high correlation exists between the bare-airframe inputs \mathbf{x} [as indicated by the coherence between the primary input x_i and secondary inputs x_j being $\gamma_{x_i x_j}^2 > 0.5$

(Ref. 2)], the matrix $\mathbf{G}_{xx}(\omega)$ will be nearly singular and cannot be inverted to complete the calculation in Eq. 3. If however, all secondary inputs x_j are all small compared to the primary input x_i [as indicated by $G_{x_j x_j} \ll G_{x_i x_i}$ 20 dB (Ref. 2)], then the secondary inputs can be ignored altogether in the analysis, treating the system as Single-Input/Single-Output (SISO). When the secondary inputs are not small, treating the system as SISO may lead to incorrect results when identifying a bare-airframe with coupled dynamics, as demonstrated for both simulation and flight test examples in Ref. 3.

For these cases of highly-correlated inputs with similar magnitudes, the MISO Direct Method can be applied using the uncorrelated (or only partially-correlated) external excitation signals (\mathbf{u} or \mathbf{v} in Fig. 1) as the input, and a post-processing step using the JIO Method is added as explained in the following section.

Joint Input-Output Method Overview

In the JIO Method, identification is done in two steps. First, the bare-airframe inputs \mathbf{x} and outputs \mathbf{y} are treated as outputs to a set of uncorrelated (or partially-correlated) reference inputs \mathbf{r} , thus identifying two frequency response matrices using the MISO Direct Approach:

$$\begin{aligned}\mathbf{H}_{rx}(\omega) &= \mathbf{G}_{rx}(\omega)\mathbf{G}_{rr}^{-1}(\omega) \\ \mathbf{H}_{ry}(\omega) &= \mathbf{G}_{ry}(\omega)\mathbf{G}_{rr}^{-1}(\omega)\end{aligned}\quad (4)$$

Then, a post-processing step is added, in which the frequency response matrices identified in the first step (Eq. 4) are used to construct the bare-airframe frequency response matrix:

$$\mathbf{H}_{xy}(\omega) = \mathbf{H}_{ry}(\omega)\mathbf{H}_{rx}^{-1}(\omega) \quad (5)$$

Since the bare-airframe input power spectral density (PSD) matrix \mathbf{G}_{xx} does not need to be inverted when using the JIO Method (Eqs. 4 and 5), the bare-airframe inputs can be highly correlated without negatively effecting the identification results. However, several conditions must be met to apply the JIO Method:

1. The individual reference inputs r_i must be at most only partially correlated (i.e., the cross-control coherence $\gamma_{r_i r_j}^2 < 0.5$ for all $i \neq j$, following the MISO Direct Method guidelines in Ref. 2), such that the PSD matrix \mathbf{G}_{rr} is invertible to complete the calculations in Eq. 4.
2. The reference input \mathbf{r} must have the same number of elements as \mathbf{x} (i.e., $\mathbf{r} \in \mathbb{R}^{n_x}$), such that the frequency response matrix \mathbf{H}_{rx} is square.

3. The individual reference inputs r_i must generate independent combinations of bare-airframe inputs \mathbf{x} , such that the matrix \mathbf{H}_{rx} is invertible to complete the calculation in Eq. 5.

Overall, the JIO Method has several advantages and disadvantages over the MISO Direct Method. The main advantage of the JIO Method is that it permits identification of MIMO systems with highly correlated inputs, as described above. A second advantage of the JIO Method (applicable to both MIMO and SISO identification, and which was its original application, Ref. 4), is that the bare-airframe frequency response estimate obtained using Eq. 5 is unbiased in the presence of correlated noise \mathbf{n} in the bare-airframe input \mathbf{x} and bare-airframe output \mathbf{y} (i.e., cases where $\mathbf{G}_{xn} \neq \mathbf{0}$ and $\mathbf{G}_{yn} \neq \mathbf{0}$). This is because the reference input \mathbf{r} can be chosen such that it is not correlated with the noise \mathbf{n} (i.e., $\mathbf{G}_{rn} = \mathbf{0}$). Correlated noise in the input and output can be caused by feedback and results in biased bare-airframe frequency response estimates using the MISO Direct Method for high levels of noise-to-signal ratio (NSR > 0.3) (Ref. 2).

The main disadvantage of the JIO Method is that the overall accuracy of the identification of \mathbf{H}_{xy} is a function of the accuracy of both \mathbf{H}_{ry} and \mathbf{H}_{rx} . Therefore, as will be discussed in the next section, the reference signal \mathbf{r} should be chosen such that it has a high signal-to-noise ratio (SNR) and high coherence with both the bare-airframe input \mathbf{x} and bare-airframe output \mathbf{y} across the frequency range of interest. This will ensure estimates of \mathbf{H}_{ry} and \mathbf{H}_{rx} with low variance, and improve the overall accuracy and coherence of \mathbf{H}_{xy} (Ref. 3).

Experimental Design for Best JIO Results

In a typical flight test, the reference inputs \mathbf{r} are excited one at a time using a frequency sweep signal for a total of n_x sets of records (accounting for repeat maneuvers for each reference inputs). Then, the i -th columns of \mathbf{H}_{rx} and \mathbf{H}_{ry} are determined from the records corresponding to the excitation of r_i as:

$$\begin{aligned}H_{r_i x_j}(\omega) &= G_{r_i x_j}(\omega)/G_{r_i r_i}(\omega) \\ H_{r_i y_j}(\omega) &= G_{r_i y_j}(\omega)/G_{r_i r_i}(\omega)\end{aligned}\quad (6)$$

After analyzing the n_x sets of records and filling in the n_x columns of \mathbf{H}_{rx} and \mathbf{H}_{ry} , the matrices are used in Eq. 5 to determine \mathbf{H}_{xy} .

There are several choices to be made when designing an experiment to collect system identification data to be processed using the JIO Method that will affect the accuracy of the results. First is the choice of where the reference signal is summed into the block diagram. A good choice

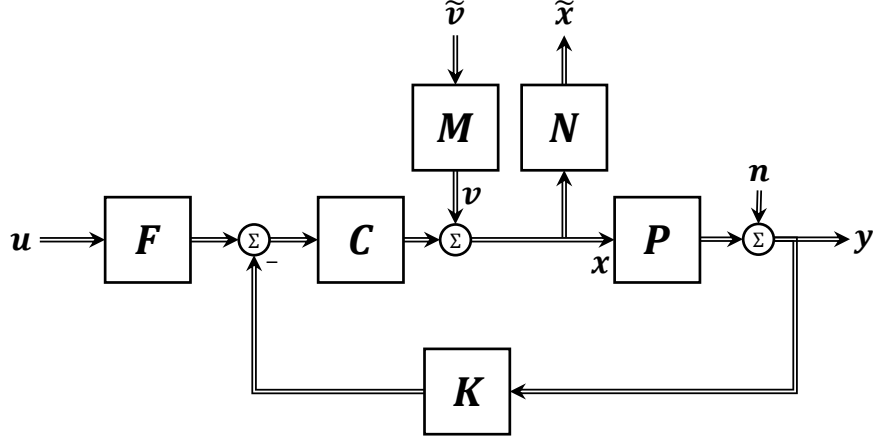


Fig. 2. Generic closed-loop block diagram with virtual effector mixing matrices M and N .

for the reference signal is the tracking command signal (\mathbf{u} in Fig. 1), because the control system will attempt to follow these commands, thus ensuring high SNR and high coherence across a large frequency range. However, for over-actuated systems such as multirotor UAS, the number of bare-airframe inputs n_x is typically greater than the number of tracking signal inputs n_u , and so n_x different excitations cannot be commanded through \mathbf{u} . In such cases, the reference signals can be summed directly into the actuator commands (\mathbf{v} in Fig. 1), which will provide the n_x different excitations.

When summing the exciting directly into the actuator commands, it is often beneficial to excite the bare-airframe inputs as symmetric and differential groups, referred to here as *virtual effectors*, to concentrate the resulting aircraft motion to one primary axis at a time. This is shown in Fig. 2, where a mixing matrix M ($n_x \times n_x$) is used to allocate the virtual effector commands \mathbf{v} to the individual actuator external commands \mathbf{v} :

$$\mathbf{v} = M\mathbf{v} \quad (7)$$

An example of virtual effectors is treating left and right flaperons on a fixed-wing aircraft as symmetric flaps and differential ailerons (e.g., Ref. 19). As such, they are typically excited as symmetric flaps to generate primarily pitch/heave motion and as differential ailerons to generate primarily roll motion, instead of exciting the individual actuators one at a time to generate coupled aircraft motion. Exciting virtual effectors instead of individual actuators helps constrain the aircraft motion to one primary axis which is beneficial to better keep the aircraft on-condition during data collection and to improve SNR in the primary axis being excited. In the case of sym-

metric aircraft, exciting virtual effectors can also help decouple the dynamics and reduce the overall system identification problem size (e.g., identifying the longitudinal and lateral/directional dynamics of a fixed-wing aircraft separately).

The next experimental design choice is the selection of the reference signals \mathbf{r} used in the JIO analysis. The reference signals are typically selected to be the same as the excitation signals used. This ensures that they are not correlated with the noise in either the bare-airframe inputs \mathbf{x} or aircraft response \mathbf{y} . The bare-airframe inputs \mathbf{x} and outputs \mathbf{y} can be expressed as functions of the reference inputs \mathbf{r} and measurement noise \mathbf{n} as:

$$\begin{aligned} \mathbf{x} &= H_{rx}\mathbf{r} + H_{nx}\mathbf{n} \\ \mathbf{y} &= H_{ry}\mathbf{r} + H_{ny}\mathbf{n} \end{aligned} \quad (8)$$

Assuming the reference inputs can be excited one at a time (which is typically the case) the individual coherence values between each reference r_i and each bare-airframe input x_j and output y_j are given by:

$$\begin{aligned} \gamma_{r_i x_j}^2 &= \frac{jH_{r_i x_j}^2 G_{r_i r_i}}{jH_{r_i x_j}^2 G_{r_i r_i} + \sum_{k=1}^{n_y} jH_{n_k x_j}^2 G_{n_k n_k}} \\ \gamma_{r_i y_j}^2 &= \frac{jH_{r_i y_j}^2 G_{r_i r_i}}{jH_{r_i y_j}^2 G_{r_i r_i} + \sum_{k=1}^{n_y} jH_{n_k y_j}^2 G_{n_k n_k}} \end{aligned} \quad (9)$$

The reference signal PSD function $G_{r_i r_i}$ is a function of the excitation signal selected, while the noise PSD function $G_{n_k n_k}$ is typically assumed flat (white noise). Therefore, high SNR and high coherence are attained when the magnitudes of $H_{r_i x_j}$ and $H_{r_i y_j}$ are large compared to $H_{n_k x_j}$.

Finally, the bare-airframe inputs used in the analysis must be selected. Here, as with the selection of the excitation signal, the choice is between individual actuators \mathbf{x} or virtual effectors $\tilde{\mathbf{x}}$ (Fig. 2), where the virtual effectors signal is constructed by use of an $n_x \times n_x$ mixing matrix \mathbf{N} :

$$\tilde{\mathbf{x}} = \mathbf{N}\mathbf{x} \quad (10)$$

which is typically set to $\mathbf{N} = \mathbf{M}^{-1}$.

When identification is done using the virtual effectors as the bare-airframe inputs, the identified bare-airframe takes the form of:

$$\tilde{\mathbf{P}} = \mathbf{H}_{\tilde{\mathbf{x}}y} \quad (11)$$

and the bare-airframe response to individual actuators can be determined as:

$$\mathbf{P} = \tilde{\mathbf{P}}\mathbf{N} \quad (12)$$

since \mathbf{N} is known.

The following section will describe the octocopter test case and show how these considerations are applied.

TEST CASES DESCRIPTION

The examples shown in this paper are based on the hover lateral axis dynamics of the octocopter UAS shown in Fig. 3(a). Similar results were obtained for the other axes, which are omitted in this paper for brevity.

Bare-Airframe Model

The octocopter UAS bare-airframe model used in this paper was identified from flight-test data. The results of the flight test system identification are presented in Refs. 20, 21, and 23, which all utilized the JIO Method. Here, the model will be used to assess the effects of reference signal selection and measurement noise on the identification results. The numbering convention, grouping, and direction of rotation of the eight motors is shown in the diagram in Fig. 3(b).

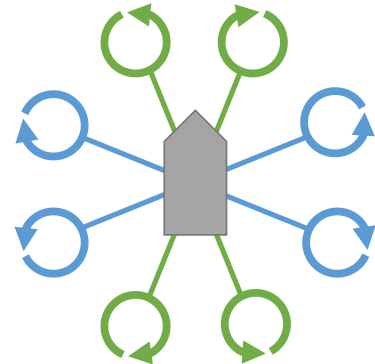
As mentioned earlier, it is often beneficial to group the individual actuators \mathbf{x} into virtual effectors $\tilde{\mathbf{x}}$ for excitation and identification purposes, which was done in the test cases presented in this paper. For the octocopter, the eight motors were first divided into a pair of tetrads (i.e., two groups of four), the first consisting of the front pair and back pair of motors [motors 1, 2, 5, and 6 in Fig. 3(b)], correspond to individual actuators x_1, x_2, x_5 , and x_6] and the second consisting of the left pair and right pair of motors [motors 3, 4, 7, and 8 in Fig. 3(b)], correspond to individual actuators x_3, x_4, x_7 , and x_8 . The eight virtual effectors were then selected to produce lateral, longitudinal, collective, and directional inputs using the Tetrad 1 motors only (virtual effectors \tilde{x}_1 – \tilde{x}_4) and the the Tetrad

2 motors only (virtual effectors \tilde{x}_5 – \tilde{x}_8). Table 1 lists the virtual effectors with their description and corresponding motor commands. The mixing matrix \mathbf{N}^{-1} used to allocate the virtual effectors to the individual actuators as shown in Fig. 2 is given by:

$$\begin{bmatrix} x_1 \\ x_2 \\ x_3 \\ x_4 \\ x_5 \\ x_6 \\ x_7 \\ x_8 \end{bmatrix} = \underbrace{\begin{bmatrix} 1 & 1 & 1 & 1 & 0 & 0 & 0 & 0 \\ 1 & 1 & 1 & 1 & 0 & 0 & 0 & 0 \\ 0 & 0 & 0 & 0 & 1 & 1 & 1 & 1 \\ 0 & 0 & 0 & 0 & 1 & 1 & 1 & 1 \\ 1 & 1 & 1 & 1 & 0 & 0 & 0 & 0 \\ 1 & 1 & 1 & 1 & 0 & 0 & 0 & 0 \\ 0 & 0 & 0 & 0 & 1 & 1 & 1 & 1 \\ 0 & 0 & 0 & 0 & 1 & 1 & 1 & 1 \end{bmatrix}}_{\mathbf{N}^{-1}} \begin{bmatrix} \tilde{x}_1 \\ \tilde{x}_2 \\ \tilde{x}_3 \\ \tilde{x}_4 \\ \tilde{x}_5 \\ \tilde{x}_6 \\ \tilde{x}_7 \\ \tilde{x}_8 \end{bmatrix} \quad (13)$$



(a)



(b)

Fig. 3. Octocopter UAV (a) picture and (b) motor numbering and rotation convention.

Figure 4 shows the octocopter bare-airframe roll rate response to Tetrad 1 Lateral virtual effector p/\tilde{x}_1 and Tetrad 2 Lateral virtual effector p/\tilde{x}_5 . The octocopter has dynamics representative of multirotor UAS, with an unstable phugoid mode at $\omega = 2.36$ rad/sec and a motor lag

Table 1. Octocopter Virtual Effectors

Virtual Effector	Description	Motor Commands	
		Increase RPM	Decrease RPM
\tilde{x}_1	Tetrad 1 Lateral Input	x_1, x_6	x_2, x_5
\tilde{x}_2	Tetrad 1 Longitudinal Input	x_1, x_2	x_5, x_6
\tilde{x}_3	Tetrad 1 Collective Input	x_1, x_2, x_5, x_6	—
\tilde{x}_4	Tetrad 1 Directional Input	x_1, x_5	x_2, x_6
\tilde{x}_5	Tetrad 2 Lateral Input	x_7, x_8	x_3, x_4
\tilde{x}_6	Tetrad 2 Longitudinal Input	x_3, x_8	x_4, x_7
\tilde{x}_7	Tetrad 2 Collective Input	x_3, x_4, x_7, x_8	—
\tilde{x}_8	Tetrad 2 Directional Input	x_3, x_7	x_4, x_8

mode at $\omega = 11.66$ rad/sec.

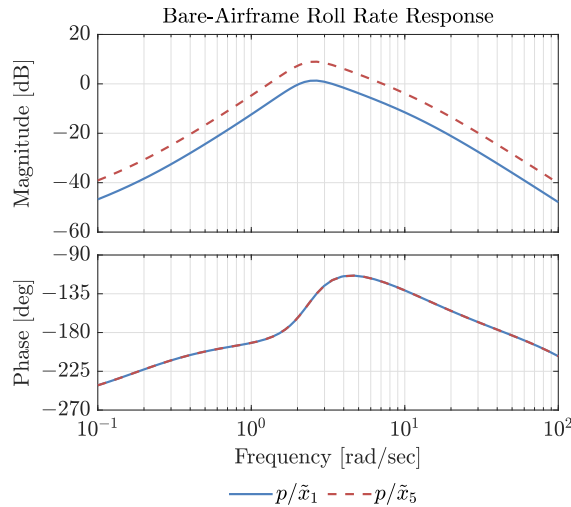


Fig. 4. Bare-airframe roll rate response to Tetrad 1 Lateral virtual effector \tilde{x}_1 and Tetrad 2 Lateral virtual effector \tilde{x}_5 (hover).

Control System

The flight-identified hover model of the octocopter was combined with an explicit model following (EMF) control system (Ref. 24) which provides an attitude-command/attitude-hold (ACAH) response type in the lateral and longitudinal axes, and a rate-command/heading-hold (RCHH) response type in the directional axis. The collective axis was left open-loop for the nominal case presented in this paper.

The control allocation matrix used in the control system \mathbf{C} takes the four control system channel commands (lateral, longitudinal, collective, and directional) and distributes them to the eight individual motors. The nominal

control allocation matrix is given by:

$$\begin{bmatrix} x_1 \\ x_2 \\ x_3 \\ x_4 \\ x_5 \\ x_6 \\ x_7 \\ x_8 \end{bmatrix} = \underbrace{\begin{bmatrix} 1/8 & 1/8 & 1/8 & 1/8 \\ 1/8 & 1/8 & 1/8 & 1/8 \\ 1/8 & 1/8 & 1/8 & 1/8 \\ 1/8 & 1/8 & 1/8 & 1/8 \\ 1/8 & 1/8 & 1/8 & 1/8 \\ 1/8 & 1/8 & 1/8 & 1/8 \\ 1/8 & 1/8 & 1/8 & 1/8 \\ 1/8 & 1/8 & 1/8 & 1/8 \end{bmatrix}}_{\mathbf{C}} \begin{bmatrix} \delta_{\text{lat}} \\ \delta_{\text{lon}} \\ \delta_{\text{col}} \\ \delta_{\text{ped}} \end{bmatrix} \quad (14)$$

which distributes the control system commands evenly to all eight motors.

Figure 5 shows the lateral axis broken-loop frequency response. The control system has a lateral axis crossover frequency of $\omega_c = 14.32$ rad/sec and gain and phase margins values that meet the stability margin requirements of SAE-AS94900 (Ref. 25). Figure 6 shows the closed-loop roll attitude frequency response to lateral stick input. For this ACAH response type, the control system has a bandwidth value (Ref. 24) of $\omega_{\text{BW}} = 9.32$ rad/sec.

Simulated Noise

The measurement noise (n in Fig. 1) is modeled by band-limited white noise to simulate real-world flight test conditions. Similar noise was added to all measurement signals with the same RMS values σ_n (in units of deg, deg/sec, and ft/sec), but different random number generator seeds. Four levels of noise were used with RMS values of $\sigma_n = 0, 1.70, 3.52$, and 5.37 , selected to give noise-to-signal ratios (NSR) of $0, 0.1, 0.2$, and 0.3 for the roll rate signal for Method 1 (described below). The NSR was calculated in the frequency domain as the ratio of roll rate signal RMS due to noise to roll rate signal RMS due

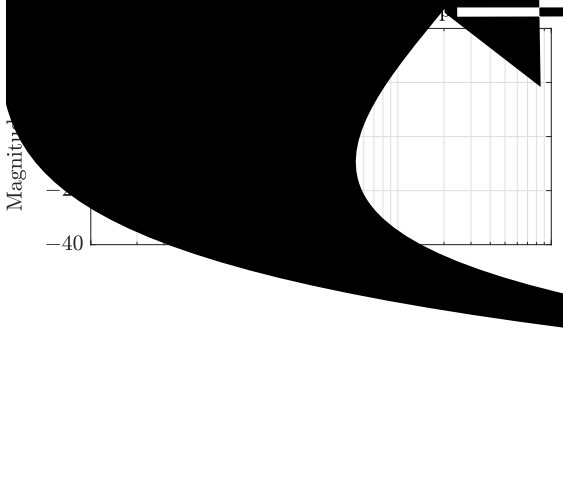


Fig. 5. Lateral axis broken-loop response (hover).

to the reference input (as in Ref. 2):

$$\text{NSR} = \frac{\sqrt{\int_{k=1}^{n_y} jH_{n_k p}^2 G_{n_k n_k} d\omega}}{\sqrt{\int jH_{r p}^2 G_{rr} d\omega}} \quad (15)$$

A maximum NSR = 0.3 was selected because it is the highest recommended NSR for closed-loop identification using the Direct Method (Ref. 2), due to the Direct Method's susceptibility to bias error when measurement noise is fed back to the bare-airframe inputs. As the JIO results presented later will show, though, the JIO Method produces unbiased frequency response estimates in the presence of noise for all NSR levels simulated here.

Identification Methods

Three identification methods relying on the JIO Method were investigated in this study and are presented in this section. In all three cases, the excitation signal magnitudes were sized to give resulting peak-to-peak aircraft outputs of $p_{\max} = 50 \text{ deg/sec}$, $q_{\max} = 5 \text{ ft/sec}^2$, and $r_{\max} = 7 \text{ deg/sec}$.

In addition to providing a description of each method, predicted analytical results of the bare-airframe input and output PSD and coherence functions with respect to the reference inputs are also presented in this section. The analytical results make the sometimes subtle differences between the three methods more clear, and are used to correlate the differences seen in the simulation results in the next section.

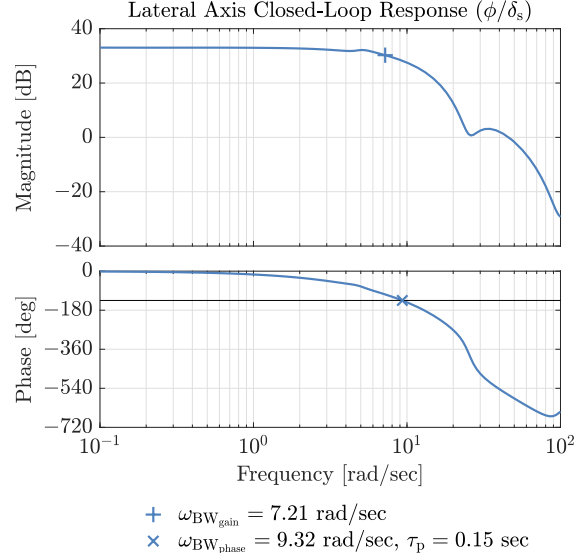


Fig. 6. Roll attitude closed-loop response to tracking command input (hover).

Method 1: Tracking Signal Sweeps, Modified Control Allocation

Method 1 uses frequency sweep excitations injected into the tracking command signal (\mathbf{u} in Fig. 2). Recall that the control laws have four channels, and therefore four tracking signals (i.e., $n_u = 4$). However, the octocopter bare-airframe to be identified has eight inputs (i.e., $n_x = 8$). Therefore, in order to use this method, the control allocation matrix \mathbf{C} (Eq. 14) must be modified to generate different combinations of bare-airframe inputs \mathbf{x} for repeated tracking signal commands. In this example, two different control allocation matrices were implemented: \mathbf{C}_1 which sends the control system perturbation motor commands to the Tetrad 1 motors only and \mathbf{C}_2 which sends the control system perturbation motor commands to the Tetrad 2 motors only. In both cases of \mathbf{C}_1 and \mathbf{C}_2 , the trim motor commands necessary to maintain the hover condition are sent to all motors. In addition, the overall loop gain was tuned to be the same for the two control allocation matrices to maintain the stability characteristics of the control system.

Two sets of four frequency sweeps were conducted, exciting each of the four control system tracking signals with \mathbf{C}_1 and then again with \mathbf{C}_2 . Table 2 contains a summary of the reference signals used in this method and the corresponding excitation axis.

Figure 7 shows the Method 1 PSD functions of the roll rate response to the reference signals r_1 and r_5 (lateral Tetrad commands), calculated analytically as:

$$G_{pp} = jH_{r_i p}^2 G_{r_i r_i} \quad (16)$$

and roll rate response to noise \mathbf{n} , calculated analytically

Table 2. Reference Inputs for Methods 1, 2, and 3

Reference	Method 1 (Tracking Signal Sweeps, Modified Control Allocation)	Method 2 (Virtual Effector Sweeps)	Method 3 (Simultaneous Sweeps)
1	u_1 (Lateral tracking command, \mathcal{C}_1)	\tilde{v}_1 (Tetrad 1 Lateral input)	$u_1 + \tilde{v}_1$
2	u_2 (Longitudinal tracking command, \mathcal{C}_1)	\tilde{v}_2 (Tetrad 1 Longitudinal input)	$u_2 + \tilde{v}_2$
3	u_3 (Collective tracking command, \mathcal{C}_1)	\tilde{v}_3 (Tetrad 1 Collective input)	$u_3 + \tilde{v}_3$
4	u_4 (Directional tracking command, \mathcal{C}_1)	\tilde{v}_4 (Tetrad 1 Directional input)	$u_4 + \tilde{v}_4$
5	u_1 (Lateral tracking command, \mathcal{C}_2)	\tilde{v}_5 (Tetrad 2 Lateral input)	$u_1 + \tilde{v}_5$
6	u_2 (Longitudinal tracking command, \mathcal{C}_2)	\tilde{v}_6 (Tetrad 2 Longitudinal input)	$u_2 + \tilde{v}_6$
7	u_3 (Collective tracking command, \mathcal{C}_2)	\tilde{v}_7 (Tetrad 2 Collective input)	$u_3 + \tilde{v}_7$
8	u_4 (Directional tracking command, \mathcal{C}_2)	\tilde{v}_8 (Tetrad 2 Directional input)	$u_4 + \tilde{v}_8$

as:

$$G_{pp} = \sum_{k=1}^{n_y} jH_{nk} p^2 G_{n_k n_k} \quad (17)$$

The figure shows similar PSD functions for Tetrad 1 Lateral input \tilde{x}_1 and Tetrad 2 Lateral input \tilde{x}_5 . The PSD functions to noise are shown for the high noise ($\sigma_n = 5.37$) case. Note that for this method, the Tetrad 2 Lateral input PSD $G_{\tilde{x}_5 \tilde{x}_5}$ for reference r_1 and the Tetrad 1 Lateral input PSD $G_{\tilde{x}_1 \tilde{x}_1}$ for reference r_5 are 0 since the control allocation matrices \mathcal{C}_1 and \mathcal{C}_2 only send the control system commands to one tetrad per set of sweeps.

Figure 8 shows the resulting coherence functions for roll rate p , Tetrad 1 Lateral input \tilde{x}_1 , and Tetrad 2 Lateral input \tilde{x}_5 for the high noise ($\sigma_n = 5.37$) case, calculated analytically using the PSD functions shown in Fig. 7 and Eq. 9. Overall this method results in high SNR and coherence for the bare-airframe output p and bare-airframe inputs \tilde{x}_1 and \tilde{x}_5 across a broad frequency range.

The main benefit of this method are that since the control system is tracking the reference signal, high SNR and coherence values are achievable across a wide frequency range (as shown in Figs. 7 and 8). A potential issue with implementing this method is that changing the control allocation scheme in the control laws may not always be possible or not practical, as it may affect the control system stability or require retuning gains.

Method 2: Virtual Effector Sweeps Method 2 uses frequency sweep excitations injected into the virtual effector commands (\mathbf{v} in Fig. 2). The virtual effector command mixing matrix \mathbf{M} is the chosen to be $\mathbf{M} = \mathbf{N}^{-1}$, as shown in Eq. 13, to excite one of the four primary degrees of freedom at a time using one of the two tetrads. Table 2 contains a summary of the reference signals used in this method and their corresponding excitation axis. Unlike Method 1 described above, here the control system control allocation matrix \mathbf{C} is not altered and the control system commands are sent to all motors (Tetrads 1 and 2)

during all sweeps. This is because even though the vehicle is excited through one virtual effector command at a time, the excitation is fed-back through the vehicle dynamics \mathbf{P} , feedback \mathbf{K} , and control system control allocation matrix \mathbf{C} to all motors.

Figure 7 shows the signal and noise PSD functions for the roll rate response p , the Tetrad 1 Lateral input response \tilde{x}_1 , and the Tetrad 2 Lateral input response \tilde{x}_5 for the two lateral reference inputs (r_1 and r_5). Overall, the roll rate PSD G_{pp} is lower for this method than Method 1. This is because when the excitation signal is summed directly into the actuator or virtual effector commands, it is treated as a disturbance by the control system which attempts to drive the aircraft motion to 0. In addition, the roll rate PSD G_{pp} is larger for the Tetrad 2 Lateral reference input r_5 than Tetrad 1 Lateral reference input r_1 , since Tetrad 2 has a larger rolling moment arm, and the same reference signal amplitude was used for both.

Figure 8 shows the resulting Method 2 coherence functions for roll rate p , Tetrad 1 Lateral input \tilde{x}_1 , and Tetrad 2 Lateral input \tilde{x}_5 for the high noise ($\sigma_n = 5.37$) case. The bare-airframe output (p) and input (\tilde{x}_1 and \tilde{x}_5) coherence functions for Method 2 are significantly less than for Method 1.

The main benefit of this method is that the control system does not need to be modified to implement it. However, this comes at the cost of reduced SNR and coherence as compared to Method 1.

Method 3: Simultaneous Sweeps Method 3 attempts to combine the benefits of both Methods 1 and 2. In this case, frequency sweep excitations are injected into the virtual effector commands (\mathbf{v} in Fig. 2) as in Method 2, to avoid having to modify the control system control allocation matrix \mathbf{C} . Therefore, the control system does not need to be modified in order to use this method. In addition, to improve the aircraft response SNR, frequency sweep excitations are simultaneously injected into the tracking signal commands that correspond to the primary

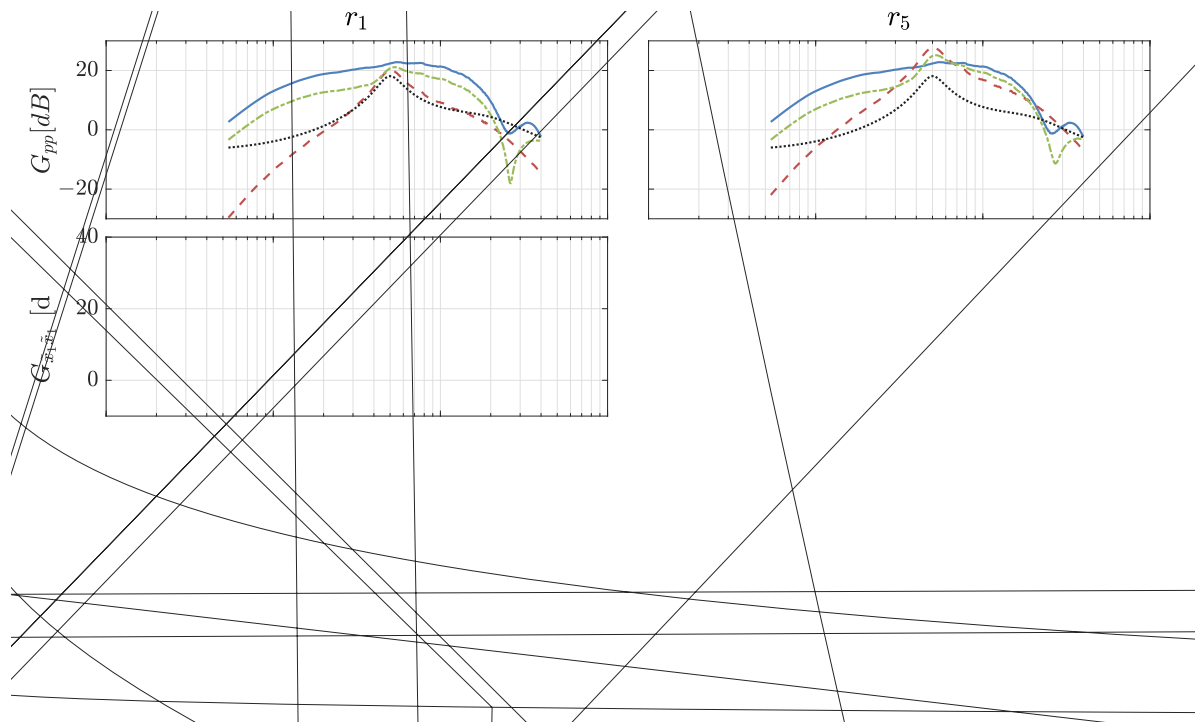


Fig. 7. Predicted power spectral density functions of roll rate p , Tetrad 1 Lateral virtual effector \tilde{x}_1 , and Tetrad 2 Lateral virtual effector \tilde{x}_5 responses to reference inputs r_1 and r_5 and noise n ($\sigma_n = 5.37$).

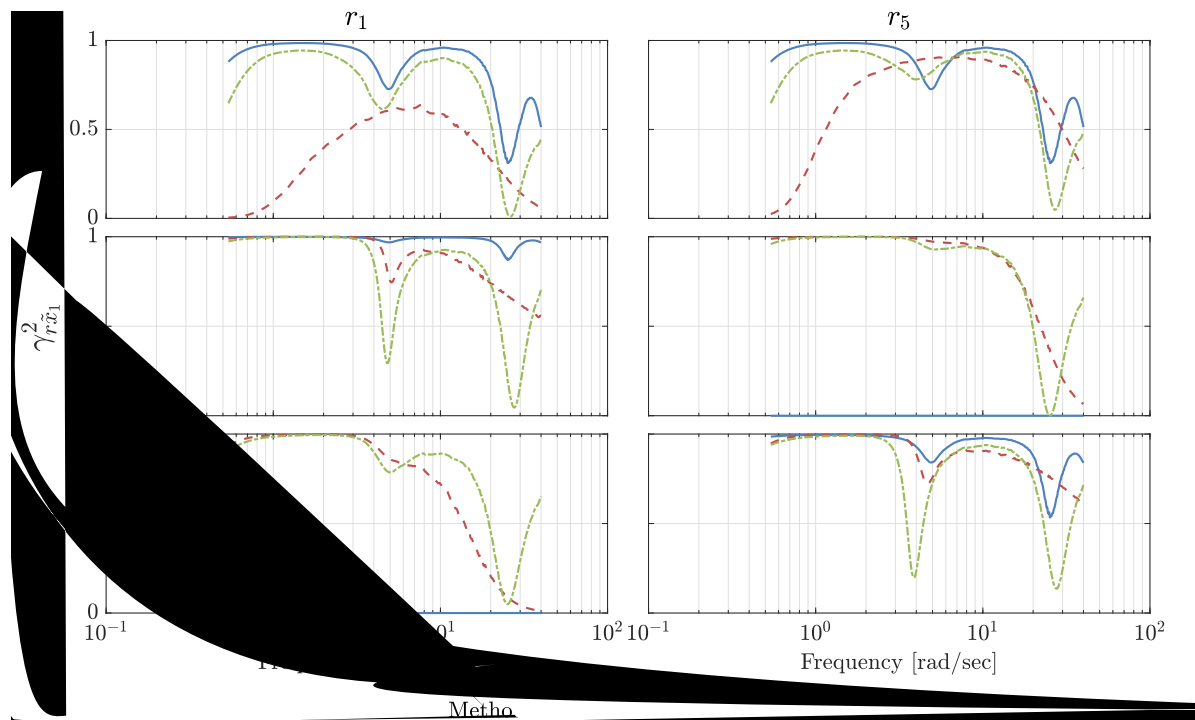


Fig. 8. Predicted coherence of roll rate p , Tetrad 1 Lateral virtual effector \tilde{x}_1 , and Tetrad 2 Lateral virtual effector \tilde{x}_5 responses to reference inputs r_1 and r_5 ($\sigma_n = 5.37$)

degree of freedom being excited. For example, when the virtual effector corresponding to Tetrad 1 Lateral input \tilde{v}_1 is being excited, the lateral axis tracking command u_1 is simultaneously excited. Similarly, when the virtual effector corresponding to Tetrad 2 Collective input \tilde{v}_3 is being excited, the collective axis tracking command u_3 is simultaneously excited.

The ratio of the excitation amplitude sent to the virtual effector commands versus that sent to the tracking signal command must be selected when using this method. When a larger ratio is sent to the tracking signal command, the bare-airframe output and input PSD functions will be larger (benefits of Method 1). However, this also results in the frequency response matrix H_{rx} having a larger condition number (with the limiting case of all the excitation signal sent to the tracking signal command resulting in a singular frequency response matrix H_{rx}). This results in the JIO calculation of Eq. 5 becoming less reliable. In the example case shown here, 50% of the magnitude of excitation used in Method 1 was sent to the tracking signal and 50% of the magnitude of excitation used in Method 2 was sent to the virtual effector commands.

Figure 7 shows the signal and noise PSD functions for the roll rate response ρ , the Tetrad 1 Lateral input response \tilde{x}_1 , and the Tetrad 2 Lateral input response \tilde{x}_5 for the two lateral reference inputs (r_1 and r_5). Overall, the bare-airframe input and output PSD functions for Method 3 approach the values for Method 1. However, as a result of the simultaneous excitation done here, at certain frequencies the two excitation signals cancel each other out due to being out of phase, which is evident in the notches present in the Method 3 PSD functions in Fig. 7 at around $\omega = 4 - 5$ rad/sec and $\omega = 20 - 30$ rad/sec.

Figure 8 shows the resulting Method 3 coherence functions for roll rate ρ , Tetrad 1 Lateral input \tilde{x}_1 , and Tetrad 2 Lateral input \tilde{x}_5 for the high noise ($\sigma_n = 5.37$) case. The bare-airframe output (ρ) and input (\tilde{x}_1 and \tilde{x}_5) coherence functions for Method 3 are overall higher than Method 2, and more similar to those for Method 1. However, coherence drops can be seen at around $\omega = 4 - 5$ rad/sec and $\omega = 20 - 30$ rad/sec, corresponding to the notches seen in the PSD functions.

The main benefits of this method are that the control system does not need to be modified to implement it, while having similar bare-airframe input and bare-airframe output SNR and coherence to Method 1. However, at certain frequencies, the two excitation signals can cancel each other out resulting in drops in SNR and coherence at those frequencies. A method to mitigate this is presented later in the Discussion section.

TEST CASE RESULTS

Figure 9 shows Method 1, 2, and 3 time histories of roll rate ρ , Tetrad 1 Lateral input \tilde{x}_1 , and Tetrad 1 Lateral input \tilde{x}_5 for the two lateral reference inputs (r_1 and r_5). The time histories shown are for the no noise case ($\sigma_n = 0$). As mentioned previously, the reference signals were sized to give a peak-to-peak roll rate of $\rho = 50$ deg/sec. Note that in the case of Methods 2 and 3, the roll rate response to reference signal r_5 is larger than the roll rate response to reference signal r_1 because reference signal r_5 excites Tetrad 2 Lateral input (Table 2) which has a larger rolling moment arm than Tetrad 1 Lateral input.

The following sections will present the identified bare-airframe roll rate frequency responses for the three methods and varying levels of noise investigated, as compared to the known simulation bare-airframe (truth) model. Note that all of the frequency response identification results shown here are for the virtual effector bare-airframe inputs (i.e., identifying H_{xy} as shown in Eq. 11). Parametric (state-space) model identification is outside of the scope of this paper, but the steps to identify a parametric model with individual actuators as the inputs, instead of virtual effectors, are as follows. First, a parametric (state-space) model is identified from frequency responses to virtual effector inputs H_{xy} . Then, the control derivative B-matrix of the identified state-space model is multiplied by the known virtual effector mixing matrix N as shown in Eq. 12, to recover the control derivatives for the individual actuators.

Fig. 9. Identified bare-airframe roll rate response to Tetrad 1 Lateral virtual effector (Method 1).

Method 1: Tracking Signal Sweeps, Modified Control Allocation

Figures 10 and 11 show the bare-airframe roll rate response to the Tetrad 1 Lateral virtual effector \tilde{x}_1 and the Tetrad 2 Lateral virtual effector \tilde{x}_5 , respectively. The figures show the actual (“truth”) bare-airframe model, as well as the Method 1 JIO identification results for the varying noise levels. Recall that the noise levels were tuned to give NSR = 0, 0.1, 0.2, and 0.3 for this method. The figures also list the mismatch cost function J (Ref. 2) and the average coherence γ_{ave}^2 for each identified response. The identified frequency responses are unbiased in the presence of noise, and even for the high noise case ($\sigma_n = 5.37$, NSR = 0.3), the mismatch costs for the two responses are $J < 30$. Mismatch costs of $J < 50$ indicate near perfect agreement between the identified response and the truth model. In addition, the average coherence for the high noise case is $\gamma_{ave}^2 > 0.7$.

The effects of noise on the identified response are largely isolated to high frequency, above $\omega \approx 20$ rad/sec, which corresponds to the frequency range at which the response PSD due to noise is of similar magnitude to response PSD due to the reference signal excitation (Fig. 7). This characteristic makes the frequency responses identified using Method 1 ideal for parametric identification of stability and control derivatives.

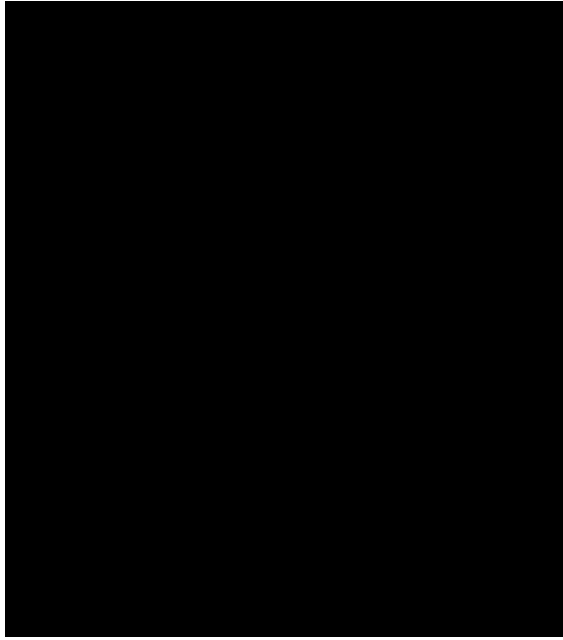


Fig. 10. Identified bare-airframe roll rate response to Tetrad 1 Lateral virtual effector (Method 1).

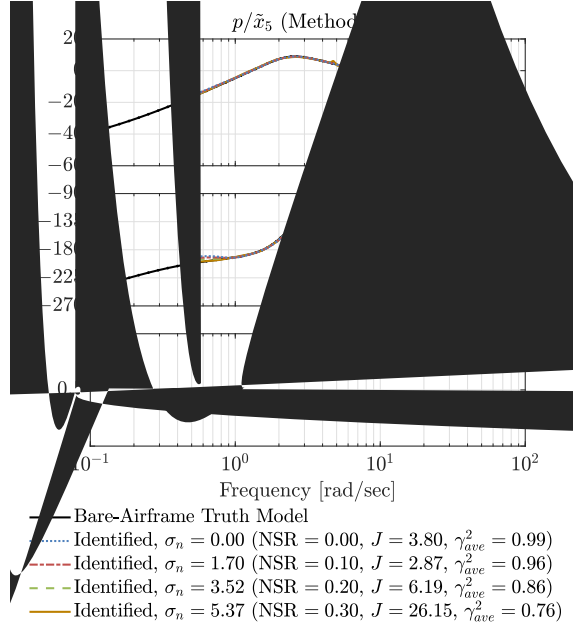


Fig. 11. Identified bare-airframe roll rate response to Tetrad 2 Lateral virtual effector (Method 1).

Method 2: Virtual Effector Sweeps

Figures 12 and 13 show the bare-airframe roll rate response to the Tetrad 1 Lateral virtual effector \tilde{x}_1 and the Tetrad 2 Lateral virtual effector \tilde{x}_5 for the truth bare-airframe model as well as the Method 2 JIO identification results for the varying noise levels. Note that the roll rate NSR ratio for Method 2 is higher than for Method 1. This is because the control system attempts to suppress the aircraft motion in this case, as opposed to tracking the reference inputs as in Method 1. The effects of this can be seen in the increased mismatch cost function J and decreased average coherence γ_{ave}^2 for the Method 2 results as compared to the Method 1 results. For Method 2, the low noise case ($\sigma_n = 1.70$), has mismatch costs $J > 100$, demonstrating that this method is less robust to noise.

In addition, the mismatch between the identified responses using Method 2 and the truth model are not just isolated to high frequency, as they were for Method 1. Large offsets can be seen at low frequency, below $\omega \approx 1$ rad/sec, which can pose an issue for use of these frequency responses for parametric identification of stability derivatives.

Method 3: Simultaneous Sweeps

Figures 14 and 15 show the bare-airframe roll rate response to the Tetrad 1 Lateral virtual effector \tilde{x}_1 and the Tetrad 2 Lateral virtual effector \tilde{x}_5 for the truth bare-airframe model as well as the Method 3 JIO identification results for the varying noise levels. Overall, the results

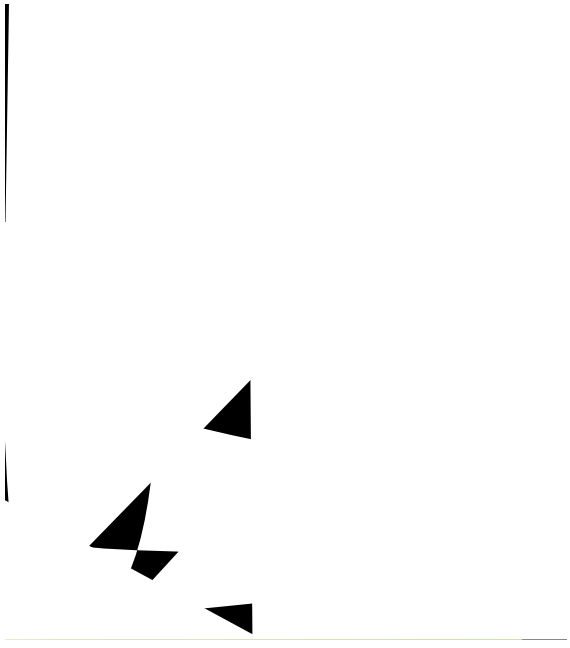


Fig. 12. Identified bare-airframe roll rate response to Tetrad 1 Lateral virtual effector (Method 2).

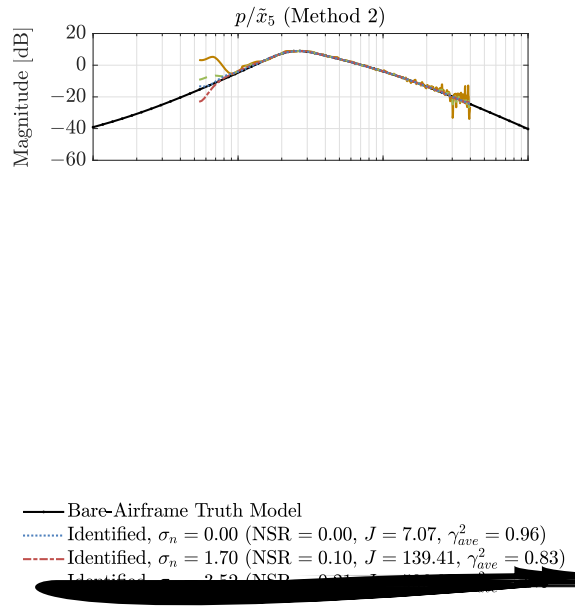


Fig. 13. Identified bare-airframe roll rate response to Tetrad 2 Lateral virtual effector (Method 2).

for Method 3 are improved over the results for Method 2, especially at the low frequency range, making the frequency responses identified using Method 3 suitable for parametric identification of stability derivatives.

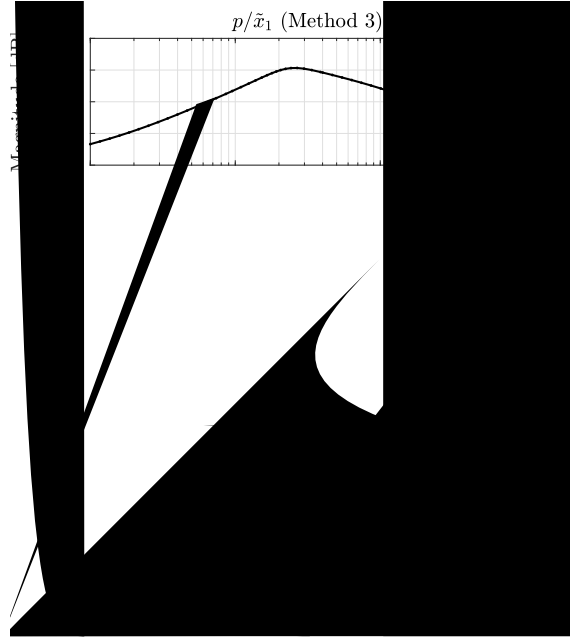


Fig. 14. Identified bare-airframe roll rate response to Tetrad 1 Lateral virtual effector (Method 3).

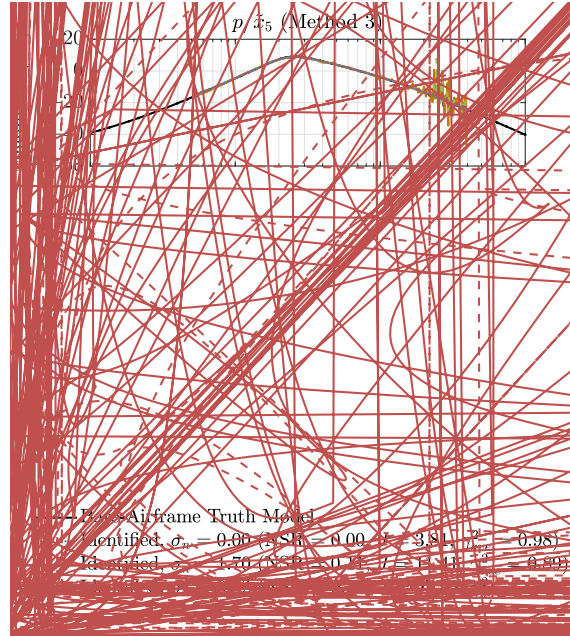


Fig. 15. Identified bare-airframe roll rate response to Tetrad 2 Lateral virtual effector (Method 3).

DISCUSSION

Method Comparison

Figures 16 and 17 show the bare-airframe roll rate response to the Tetrad 1 Lateral virtual effector \tilde{x}_1 and the Tetrad 2 Lateral virtual effector \tilde{x}_5 for the high noise case ($\sigma_n = 5.37$) for all three methods. The comparison here clearly shows the improved accuracy of Method 1 and Method 3 at low frequency. This makes Method 3 a good alternative when the control system control allocation matrix \mathbf{C} cannot be modified.

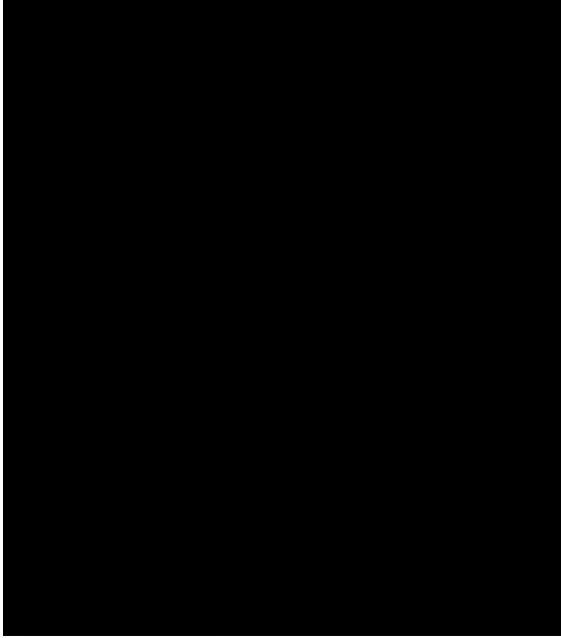


Fig. 16. Comparison of identified bare-airframe roll rate response to Tetrad 1 Lateral virtual effector (Methods 1, 2, and 3)

However, the results for Method 3 are worse than Method 2, in terms of variance in the identified frequency response, at high frequency ($\omega > 10$ rad/sec), and have lower coherence than Method 2 at high frequency and around $\omega = 4 - 5$ rad/sec. These regions correspond to the notches seen in response PSD functions in Fig. 7 for Method 3 at around $\omega = 4.5$ and 25 rad/sec. The presence of these notches, and potential ways to mitigate them, can be understood by examining the bare-airframe input and output responses to the reference input for Method 3. From Eqs. 2, 7, and 10, the bare-airframe input and output frequency responses to the Method 3 reference inputs are:

$$\begin{aligned} H_{ry} &= (\mathbf{I} + \mathbf{PCK})^{-1} \mathbf{P}(a\mathbf{CF} + b\mathbf{M}) \\ H_{r\tilde{x}} &= \mathbf{N}(\mathbf{I} + \mathbf{CKP})^{-1}(a\mathbf{CF} + b\mathbf{M}) \end{aligned} \quad (18)$$

Fig. 17. Comparison of identified bare-airframe roll rate response to Tetrad 2 Lateral virtual effector (Methods 1, 2, and 3).

where a and b are the ratios of the reference input sent to the tracking command \mathbf{u} and virtual effector command $\tilde{\mathbf{v}}$ respectively. Notches will be present in the frequency responses where the magnitude of $a\mathbf{CF} + b\mathbf{M}$ is small (i.e., where $a\mathbf{CF} \approx b\mathbf{M}$). One way to mitigate this is to introduce a lead-lag filter L on the part of the reference signal sent to the virtual effector command, to add phase at the frequencies where $a\mathbf{CF} + b\mathbf{M}$ is small, making the magnitude of $a\mathbf{CF} + bL\mathbf{M}$ larger at those frequencies. Prior knowledge of \mathbf{F} , \mathbf{C} , and \mathbf{M} is required to tune the notch filter L to the appropriate frequency, and care must be taken to not introduce notches at different frequencies.

Figure 18 shows the bare-airframe roll rate response to Tetrad 2 Lateral virtual effector p/\tilde{x}_5 identified using Method 3 with no lead-lag and Method 3 with a lead-lag filter implemented on the reference signal summed into the virtual effector commands. The lead-lag filter was tuned to produce 35 deg of phase lead at $\omega = 25$ rad/sec and improves the mismatch cost significantly from $J = 252.8$ to $J = 69.46$. In addition, the high frequency coherence of the identified response is slightly improved with the addition of the lead-lag filter.

When neither Method 1 nor Method 3 can be implemented in flight test, a good alternative is to first use Method 1 with a fixed control system control allocation matrix \mathbf{C} to obtain the frequency response matrix from the input to the control allocation to the aircraft output, corresponding to identification of \mathbf{PC} , using the standard MISO Direct Method. Since the control system tracks the

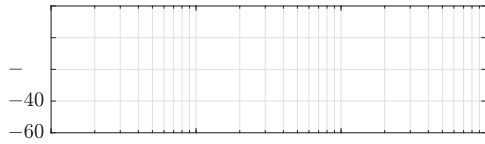


Fig. 18. Comparison of identified bare-airframe roll rate response to Tetrad 2 Lateral virtual effector (Method 3 with and without lead-lag).

reference inputs for Method 1, these identified responses are expected to have high coherence and low variance, especially at low frequency, making them ideal for identification of the stability derivatives. But these responses can only be used to identify *lumped control derivatives* that include the control allocation matrix. Then, to identify the control derivatives associated with the individual bare-airframe inputs, a second set of data is collected using Method 2 and frequency responses are identified using the JIO Method. These frequency responses can be used to identify the individual control derivatives while holding the previously identified stability derivatives fixed.

Effects of Altitude Hold

The results presented thus far were simulated with a control system that provides an ACAH response type in the lateral and longitudinal axes, an RCHH response type in the directional axis, and open-loop in the collective axis. An investigation was also done using a vertical rate command/altitude-hold response type in the collective axis. For actual flight testing, it would be easier to remain on-condition with an altitude hold mode engaged, and allow the pilot/operator to focus on the axis being excited without having to worry about maintaining altitude. However, the bare-airframe collective input response with altitude hold engaged is nonlinear to pitch and roll sweeps (even though the aircraft response to collective is linear), as positive collective is required

to maintain altitude for both positive and negative pitch and roll motion. Recall that the overall accuracy of identification results obtained with the JIO Method require that both the bare-airframe outputs and inputs have high coherence with respect to the reference inputs. The non-linear collective input response to pitch and roll reference inputs results in lower coherence and increased variance in the identified frequency responses when altitude hold mode is engaged.

Figure 19 shows the mismatch cost \mathcal{J} and average coherence γ_{ave}^2 for the bare-airframe roll rate response to the Tetrad 1 Lateral virtual effector \tilde{x}_1 and the Tetrad 2 Lateral virtual effector \tilde{x}_5 for Method 1 with and without altitude hold engaged as a function of noise RMS σ_n . The identification results with altitude hold mode engaged have higher mismatch costs and decreased coherence, especially for the higher noise cases. This suggests that system identification flight testing should be done with altitude hold modes disengaged to improve the identification results.

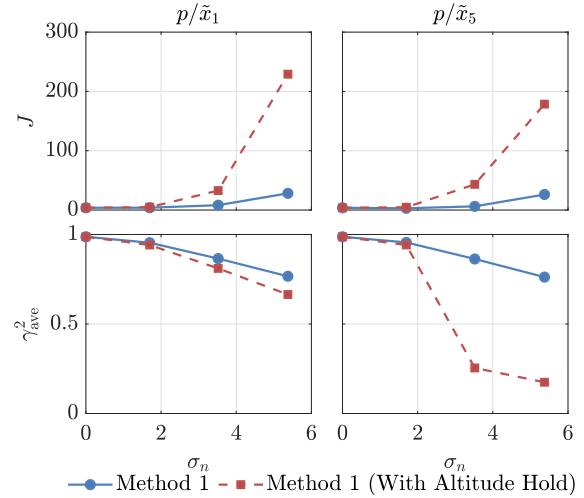


Fig. 19. Effect of altitude hold on fit cost and average coherence of identified roll rate response to Tetrad 1 and Tetrad 2 Lateral virtual effectors (Method 1).

Guidelines

Based on the results and discussion presented in this paper, the following guidelines for performing system identification of multirotor vehicles using the JIO Method are recommended:

1. When possible, bare-airframe inputs should be grouped into virtual effectors during excitation and analysis to concentrate vehicle responses to particular axes.

2. In order to apply the JIO Method, the same number of independent excitations (reference inputs) are needed as bare-airframe inputs.
3. Reference signals should be selected to have high signal-to-noise ratios (SNR) and high coherence with both the bare-airframe inputs and outputs, since the overall accuracy of the identification results obtained with the JIO Method is a function of the accuracy of the reference signal to bare-airframe inputs and reference signal to bare-airframe outputs frequency responses.
4. When the control system control allocation matrix can be modified, exciting the aircraft through the tracking signal commands (Method 1) yields identification results that are accurate over a large frequency range in the presence of noise. Frequency responses identified using tracking signal command excitation are suitable for identifying both stability and control derivatives.
5. When the control system control allocation matrix cannot be modified, simultaneous excitations summed into the virtual effector commands and corresponding tracking signal commands (Method 3) yields identification results with a similar level of accuracy as Method 1. In certain cases, the simultaneous excitations can cancel each other out at particular frequencies, which can be mitigated by the addition of a lead-lag filter on one of the excitation signals.
6. When the control system control allocation matrix cannot be modified and simultaneous excitations cannot be performed, two sets of system identification data should be gathered. First, the tracking signal commands should be excited and the data used to identify a bare-airframe model with lumped control derivatives that include the control system control allocation matrix. Then, excitations should be summed into the virtual effector commands and the data used to identify the individual actuator control derivatives while holding the previously identified stability derivatives constant.
7. Finally, altitude hold modes should be disabled when collecting system identification data for use with the JIO Method.

CONCLUSIONS

This paper presented an overview of the Joint Input-Output (JIO) Method for system identification which is a post-processing step on the frequency responses identified using the Multi-Input/Single-Output (MISO) Direct

Method and is necessary when the bare-airframe inputs are highly correlated. A simulation test case based on an octocopter UAS was used to demonstrate the JIO Method results for three different methods of vehicle excitation. The following conclusions are supported by the results:

1. Frequency responses extracted from closed-loop simulation data with highly-correlated bare-airframe inputs using the JIO Method showed excellent agreement with the truth bare-airframe model. This validates the JIO Method's ability to extract accurate MIMO bare-airframe frequency response matrices from data with highly-correlated bare-airframe inputs.
2. Frequency responses identified using the JIO Method are unbiased in the presence of measurement noise up to the maximum noise-to-signal ratio (NSR) of 0.3 tested. Mismatch costs as low as $J = 26$ were obtained between the identified frequency responses and the truth bare-airframe model for NSR = 0.3.
3. For a fixed level of measurement noise, exciting the closed-loop system with a reference signal input at the tracking command (referred to as Method 1 in this paper) results in higher bare-airframe input and output signal-to-noise ratios (SNR) and coherence with respect to the reference signals, than when exciting the closed-loop system directly at bare-airframe input (referred to as Method 2). This results in identified bare-airframe frequency responses with higher coherence and less variance in the presence of noise.
4. The presented guidelines for performing system identification of multirotor vehicles using the JIO Method are recommended for best identification results.

REFERENCES

¹Knapp, M. E., Ivler, C. M., Horn, J. F., Johnson, E. N., Bridges, D., Lopez, M., Tischler, M. B., Wagster, J., and Cheung, K., "Development and Simulation of Damage Tolerant Control Laws for a Compound Helicopter," Proceedings of the AIAA SciTech Forum, Orlando, FL, January 2020.

²Tischler, M. B. and Remple, R. K., *Aircraft and Rotorcraft System Identification: Engineering Methods with Flight Test Examples*, 2nd Ed., AIAA, Reston, VA, 2012.

³Berger, T., Tischler, M. B., Knapp, M. E., and Lopez, M. J. S., "Identification of Multi-Input Systems in the Presence of Highly Correlated Inputs," *Journal of*

Guidance, Control, and Dynamics, Vol. 41, (10), 2018, pp. 2247–2257.

⁴Akaike, H., “Some Problems in the Application of the Cross-Spectral Method,” in *Spectral Analysis of Time Series* (ed. B. Harris), 81–107, John Wiley, New York, 1967.

⁵Geary, R. C., “Relations Between Statistics: The General and the Sampling Problem When the Samples Are Large,” Proceedings of the Royal Irish Academy. Section A: Mathematical and Physical Sciences, Vol. 49, 1943.

⁶Reiersøl, O., *Confluence Analysis by Means of Instrumental Sets of Variables*, Ph.D. thesis, Stockholm College, 1945.

⁷Davall, P. W., *Applications of Statistics in the Spectral Analysis of Time-Varying Systems*, Ph.D. thesis, University of Warwick, 1975.

⁸Wellstead, P. E., “Reference Signals for Closed-Loop Identification,” *International Journal of Control*, Vol. 26, (6), 1977, pp. 945–962.

⁹Gustavsson, I., Ljung, L., and Söderström, T., “Identification of Processes in Closed Loop—Identifiability and Accuracy Aspects,” *Automatica*, Vol. 13, (1), 1977, pp. 59–75.

¹⁰Ng, T.-S., Goodwin, G. C., and Anderson, B. D. O., “Identifiability of MIMO Linear Dynamic Systems Operating in Closed Loop,” *Automatica*, Vol. 13, (5), 1977, pp. 477–485.

¹¹Anderson, B. D. O. and Gevers, M. R., “Identifiability of Closed Loop Systems Using the Joint Input-Output Identification Method,” *IFAC Proceedings Volumes*, Vol. 12, (8), 1979, pp. 645–652.

¹²Brethauer, G., “New Results for the Joint Input-Output Identification Method,” *IFAC Proceedings Volumes*, Vol. 14, (2), 1981, pp. 693–697.

¹³Brethauer, G., Gamaleja, T., and Wilfert, H.-H., “Identification of Parametric and Nonparametric Models for MIMO Closed Loop Systems by the Correlation Method,” *IFAC Proceedings Volumes*, Vol. 17, (2), 1984, pp. 753–758.

¹⁴Mitchell, L. D., Cobb, R. E., Deel, J. C., and Luk, Y. W., “An Unbiased Frequency Response Function Estimator,” Proceedings of the International Modal Analysis Conference V, London, England, April 1987.

¹⁵Cobb, R. E. and Mitchell, L. D., “Estimation of Uncorrelated Contents in Experimentally Measured FRF’s Using Three Measurement Channels,” Proceedings of the International Modal Analysis Conference VI, Orlando, Florida, February 1988.

¹⁶Cobb, R. E. and Mitchell, L. D., “A Method for the Unbiased Estimate of System FRFs in the Presence of Multiple Correlated Inputs,” Proceedings of the International Modal Analysis Conference VI, Orlando, Florida, February 1988.

¹⁷Gennaretti, M., Gori, R., Serafini, J., Bernardini, G., and Cardito, F., “Rotor dynamic wake inflow finite-state modelling,” Proceedings of the 33rd AIAA Applied Aerodynamics Conference, Dallas, TX, June 2015.

¹⁸Hersey, S., Celi, R., Juhasz, O., Tischler, M. B., Rand, O., and Khromov, V., “State-Space Inflow Model Identification and Flight Dynamics Coupling for an Advanced Rotorcraft Configuration,” Proceedings of the American Helicopter Society 73rd Annual Forum, Fort Worth, TX, May 2017.

¹⁹Knapp, M. E., Berger, T., Tischler, M. B., and Cotting, M. C., “Development of a Full Envelope Flight Identified F-16 Simulation Model,” Proceedings of the AIAA Atmospheric Flight Mechanics Conference, Kissimmee, FL, January 2018.

²⁰Berger, T., Tischler, M. B., Knapp, M. E., and Lopez, M. J. S., “Identification of Multi-Input Systems in the Presence of Highly Correlated Inputs,” Proceedings of the AIAA SciTech Forum, San Diego, CA, January 2019.

²¹Lopez, M. J. S., Tischler, M. B., Juhasz, O., Gong, A., Sanders, F. C., and Walan, A. M. G., “Development of a Reconfigurable Multicopter Flight Dynamics Model from Flight Data Using System Identification,” Proceedings of the 8th Biennial Autonomous VTOL Technical Meeting, Mesa, AZ, January 2019.

²²Berrigan, C., Lopez, M. J. S., Ruckel, P., and Prasad, J. V. R., “Bell V-280 System Identification and Model Validation with Flight Test Data using the Joint Input-Output Method,” Proceedings of the Vertical Flight Society 76th Annual Forum & Technology Display, Virginia Beach, VA, October 2020.

²³Gong, A., Hess, R., and Tischler, M., “System Identification and Full Flight-Envelope Model Stitching of a Package-Delivery Octocopter,” Proceedings of the AIAA SciTech Forum, San Diego, CA, January 2019.

²⁴Tischler, M. B., Berger, T., Ivler, C. M., Mansur, M. H., Cheung, K. K., and Soong, J. Y., *Practical Methods for Aircraft and Rotorcraft Flight Control Design: An Optimization-Based Approach*, AIAA, 2017.

²⁵Anon., “Aerospace - Flight Control Systems - Design, Installation and Test of Piloted Military Aircraft, General Specification For,” SAE-AS94900, July 2007.